REVISION

Direct and Indirect Light Energy Harvesting with Films of Ambiently Deposited ZnO Nanoparticles

Kallyni Irikura [a,b,c] *, Frank Marken [c], Philip J. Fletcher [d], Gabriele Kociok-Köhn [d], and Maria Valnice Boldrin Zanoni [a,b]

[a] *São Paulo State University (Unesp), Institute of Chemistry, Araraquara*

[b] *National Institute of Alternative Technologies for Detection, Toxicological Evaluation and Removal of Micropollutants and Radioactive Substances (INCT-DATREM), São Paulo State University (Unesp), Institute of Chemistry, Araraquara*

[c] *University of Bath, Department of Chemistry, Bath BA2 7AY, UK*

[d] *University of Bath, Materials and Chemical Characterisation Facility MC^2, Bath BA2 7AY, UK*

To be submitted to Applied Surface Science

*Corresponding author. Tel.: +55 16 33019740; E-mail address: kallyni.irikura@unesp.br or kallyni@gmail.com

Abstract

Indirect photoelectrochemical processes are possible when employing a palladium film to separate photochemical and electrochemical reactions. Here, an exploratory indirect photoelectrochemical system is developed based on ZnO or Pt@ZnO nanoparticle photocatalysts ambiently deposited onto platinum, glassy carbon, or palladium membrane electrodes and exposed to blue (385 nm) LED light in the presence of glucose hole quencher (in aqueous NaCl). It is demonstrated that under these conditions photo-excitation followed by charge transport of conduction band electrons via inter-grain conduction across ZnO particles triggers the photo-current responses. The conduction band electrons then trigger formation of interstitial hydrogen in a palladium membrane. Transport of the hydrogen across the palladium membrane into the electrochemical compartment occurs within 1-2 minutes of switching on the light. A proof-of-principle fuel cell with oxygen gas diffusion electrode (cathode) and indirect photo-anode is shown to operate with up to 28 μW cm^{-2} power output during illumination. Important power-limiting parameters and suggestions for future improvements are discussed.

Graphical abstract

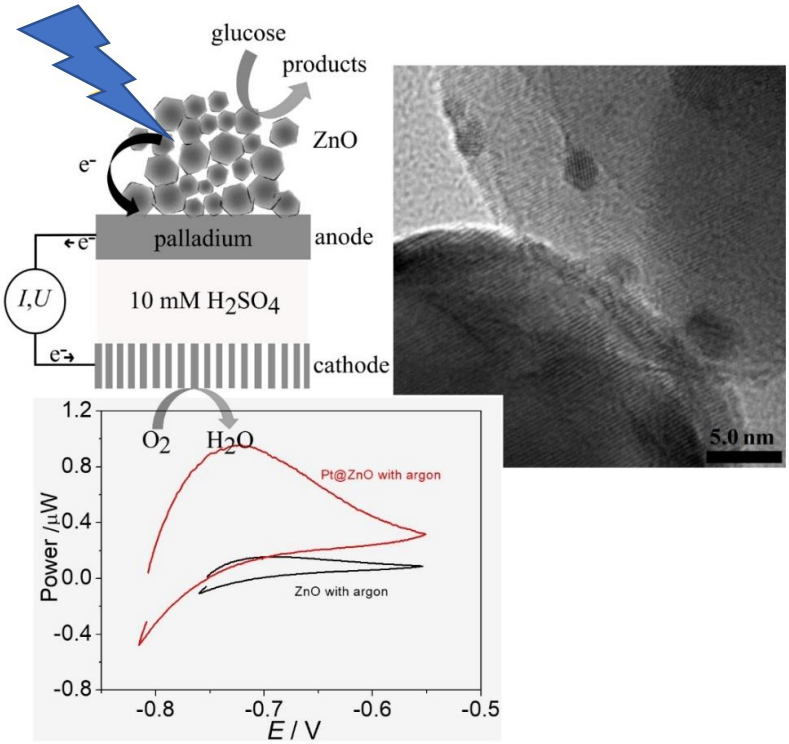

Keywords: ZnO nanoparticles, Pt@ZnO, palladium membrane, photocatalytic hydrogen generation, glucose

1. Introduction

Hydrogen is a gaseous energy-vector widely used in various industrial fields [1,2]. In the petroleum industry hydrogen is used in processes such as hydrocracking, hydro-desulfurization and hydro-dealkylation [3,4]. Nowadays, hydrogen produced from renewable resources has been identified as a sustainable alternative energy carrier to relieve environmental problems and to lower the dependence on conventional fossil fuels. In particular, hydrogen used in proton exchange membrane fuel cells is attractive due the efficiency of the energy conversion without the release of greenhouse gases [4]. In contrast to processes based on bulk-scale hydrogen, it is possible to also employ hydrogen as energy-vector on microscopic scale coupled for example to photocatalysis.

In this study, we used a commercial nano-ZnO photocatalyst (MZ-300, Tayca, Japan) with nominally 35 nm diameter and 30 m^2g^{-1} surface area [5]. ZnO exhibits unique physical and (photo-)chemical properties and a band gap in the near ultraviolet [6,7]. However, it is known that the photo-current generation efficiency of ZnO can be low due to a high recombination rate of the photo-generated e^-/h^+ pairs [8,9]. To enhance the photocatalytic performance of the ZnO either hole quenchers can be added and/or photo-deposition of platinum nanoparticles has been suggested to help improve the charge separation and the hydrogen evolution reaction [10,11].

Recently, the concept of an indirectly driven photoelectrochemical process has been proposed [12] based on the idea of separating the photoelectrochemical process and the electrolytic process with a thin palladium membrane. The key benefit of the indirect *versus* the direct photoelectrochemical process is in the possibility to employ different solution compositions for photocatalysis (e.g. with biomass) and for electrochemical energy conversion (e.g. with pure mineral acids). Hydrogen provides the “micro-energy vector” connecting photocatalysis through hydrogen-permeable palladium with the electrochemical reaction. The concept is based on a photo-redox process producing hydrogen at the surface of nanoparticles (e.g. for Pt@g-C_3N_4 [12] or here for Pt@ZnO [13]) deposited onto a palladium membrane. Under illumination and in the presence of glucose hole quencher, hydrogen is produced locally as energy carrier and transported towards a palladium membrane where hydrogen is readily absorbed. Once bound into palladium, the hydrogen can be transferred to the opposite side of the film and released in an electrochemical process [4,14,15]. This happens in contact with

electrolyte solution, where discharge of hydrogen produces protons (in aqueous acid). This anodic process can be coupled to a cathodic gas diffusion electrode where oxygen is reduced (see Fig. 1). Overall, the photo-redox process in the presence of a quencher such as glucose (here chosen to represent biomass) can be shown to transform power via hydrogen transport through palladium [16].

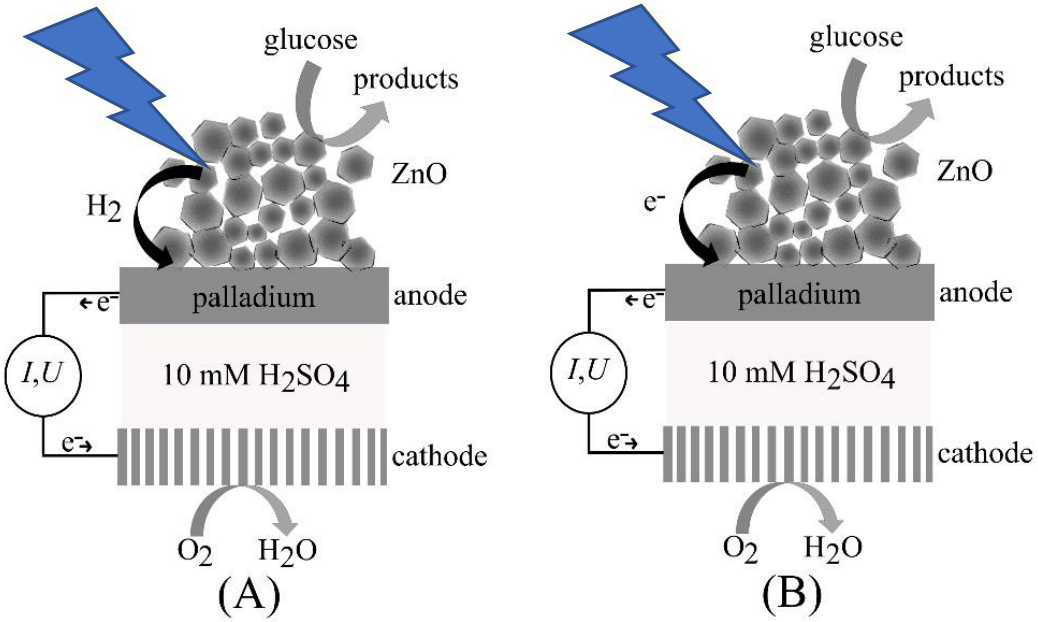

Figure 1 – Schematic illustration of an indirectly driven photoelectrochemical cell based on (A) hydrogen generation and transfer to a palladium membrane and (B) electron generation and transfer to a palladium membrane.

A peculiar mechanistic issue arises for this type of reaction sequence when either the production of hydrogen (see Figure 1A) or the production of electrons (see Figure 1B) can be responsible for the uptake of hydrogen into the palladium membrane. Although the mechanism based on hydrogen may appear more plausible, it is shown here that in fact the mechanism based on electronic transport appears to dominate for ZnO. Ambiently deposited ZnO nanoparticles are investigated (and compared to Pt@ZnO nanoparticles) and transport via electron hopping is shown to be effective without sintering of the ZnO nanoparticles. Factors such as surface conductivity, surface poisoning, glucose concentration, substrate effects, and electrolyte effects are considered. In addition to the previous reports on indirect photoelectrochemical processes [12], this constitutes a new case at the level of proof-of-principle.

2. Experimental

2.1. Chemical Reagents. All reagents were used without further purification. Deionised water (CE Instruments Ltd ultra-pure water system 18.2 MΩ cm at 22 ± 2 °C) was used for the preparation of all solutions.

2.2. Procedure for Pt@ZnO. The Pt@ZnO powder was produced from of mixture containing 20 mg ZnO (Tayca Corporation MZ-300 lot N. 300194) and 0.3 mg K_2PtCl_6 (Sigma-Aldrich) dispersed in 20 mL H_2O and 2 mL methanol (VWR Chemicals). This mixture was inserted in a glass container with magnetic stirring and illuminated for 20 h using a power LED (λ = 385, ca. 100 $mWcm^{-2}$, Thorlabs, UK). The coloration of ZnO changes from white to grey. After of the synthesis of the Pt@ZnO, it was separated, washed with ethanol, centrifuged (Eppendorf 5804-R) and dried at room temperature. Heat treatments were performed at 200 °C and at 400°C in an open tube furnace (Elite Thermal Systems Ltd TSH 12/65/550) for 2h.

2.3. Instrumentation. The characteristic powder patterns in the 2θ range from of 20° to 95° were obtained by X-ray diffraction (PXRD) with a STADI P system with Cu Kα1 radiation (1.5406 Å). Transmission electron microscopy (TEM) images were obtained with a JEOL JEM-2100Plus system equipped with an Oxford Instruments X-Max^N TSR Windowless Energy dispersive X-ray analyser (EDX).

Electrochemical measurements were performed with an Autolab PGSTAT using GPES software (Metrohm, UK). Cyclic voltammetry measurements were carried out over a potential range from +0.6 V to –0.8 V *vs.* SCE and with a scan rate of 50 mV s^{-1} without and with application of pulsed light (1 s off and 2 s on) using a power LED (λ = 385, approx. 100 $mWcm^{-2}$, Thorlabs, UK). For initial measurements at platinum or glassy carbon disk electrodes (3 mm diameter, BASi), a three-electrode cell was employed with a saturated calomel (SCE, Radiometer, Copenhagen) reference electrode and a platinum wire counter electrode (Advent Materials, UK) as illustrated in the Fig. 2A. The working electrode was prepared by deposition of a volume of 2-16 μL of a mixture of 6 mg of ZnO or Pt@ZnO in 1 mL of 1:1 v/v ethanol (VWR Chemicals) and H_2O.

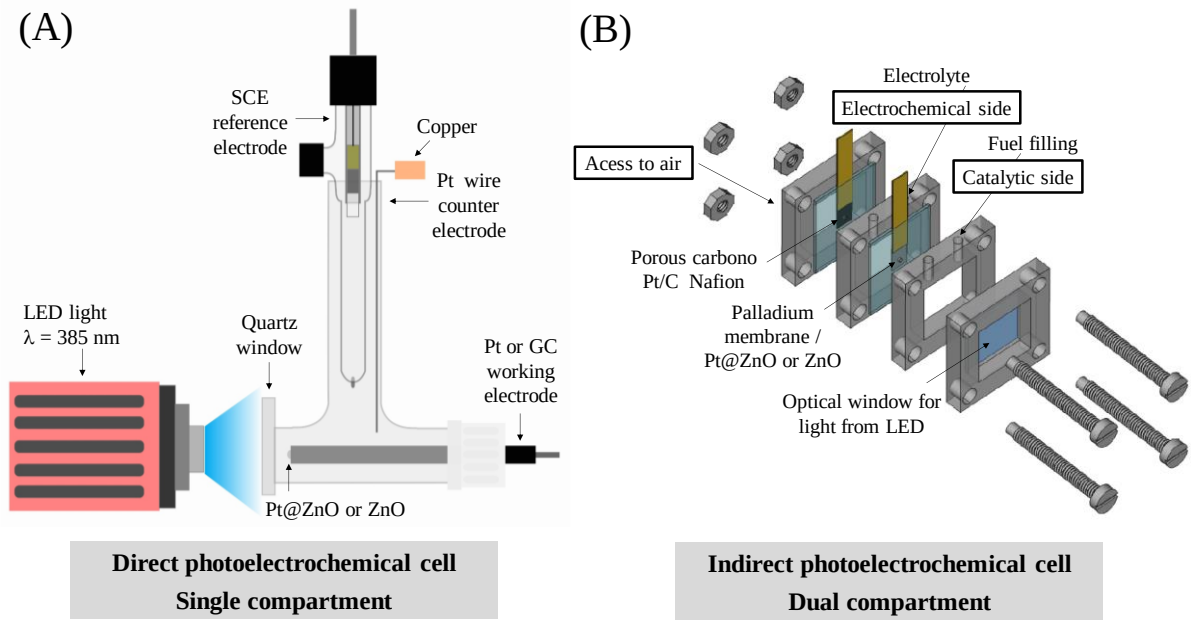

Figure 2 – (A) Experimental system for three-electrode measurements (platinum disk working electrode, SCE reference, Pt wire counter electrode) with a single compartment for the photo-electrochemical measurements. (B) Schematic drawing of the 3D-printed cell for two-electrode measurements with a fuel or catalysis side for the photochemical process, a palladium membrane/working electrode to allow transport of hydrogen, an electrochemical compartment with electrolyte, and an oxygen breathing gas diffusion electrode.

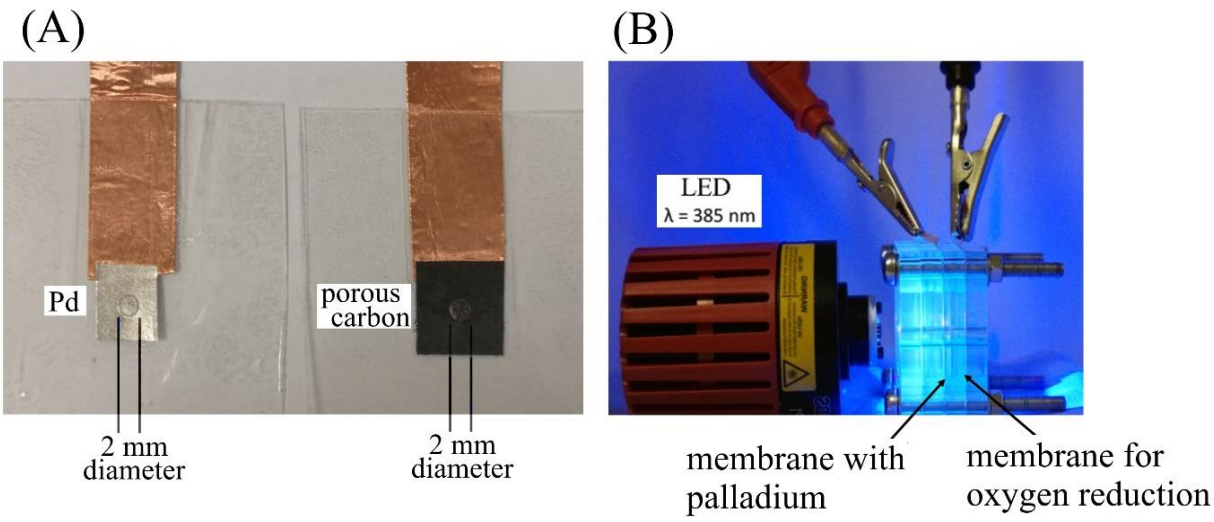

Figure 3 – (A) Laminated film electrodes based on 0.025 mm thickness palladium and 0.11 mm thickness porous carbon (Toray 030). (B) Photographic image of the illuminated 3D-printed two-compartment indirect photo-electrochemical cell.

Zero current chronopotentiometry and chronoamperometry experiments were performed in an indirect photo-fuel cell according to the illustration in Fig. 2B. The electrodes were prepared using copper tape to provide electric contact and thermal lamination film (polypropylene film) to leave exposed only an area of 2 mm diameter on both sides and for

both types of electrodes. Porous carbon (Toray Paper 030, see Fig. 3A) was used as cathode and modified with 6 μL of a mixture of 5 mg Pt/C catalyst **(**HISPEC 4000, Johnson Matthey, 40 wt% Pt) dispersed in 1 mL isopropanol and 2 μL of Nafion 117 solution (5 wt%, Aldrich) to improve the proton mobility when the oxygen is reduced and to keep the catalyst on the carbon membrane. As anode was used palladium membrane (Goodfellow, 0.025 mm thickness, optically tested) modified with 4 μL of the mixture of ZnO or Pt@ZnO dispersed in ethanol/H_2O (usually 6 mg solid per mL of ethanol/H_2O 1:1). A solution of 10 mmol L^{-1} H_2SO_4 was inserted in the electrochemical compartment and a solution of 500 mmol L^{-1} glucose in 10 mmol L^{-1} NaCl was filled into the catalytic compartment. Measurements were conducted at open circuit potential (OCP), with light irradiation (λ = 385 nm) for 950s, either in ambient air or with argon de-aeration. Subsequently, cyclic voltammetry measurements were carried out starting at OCP with a scan rate of 1 mV s^{-1} to give information about the fuel cell power generation.

3. Results and Discussion

3.1. Production and Characterisation of ZnO and Pt@ZnO Nanophotocatalysts

ZnO and Pt@ZnO materials were employed with and without initial heat treatment to make photo-electrochemical experiments more reproducible. A mild 200 ^oC heat treatment seemed to give the most encouraging results (*vide infra*; also see data in Fig. S1). The morphology of the ZnO or Pt@ZnO powders with 2 h heat treatment at 200 °C in air was characterised by TEM (additional data for materials without heat treatment with 200 ^oC and 400 ^oC treatment are essentially identical as shown in Fig. S2). In Fig. 4A and 4B a mixed morphology can be seen with spherical, hexagonal and elongated hexagonal shapes, which suggest some aggregation and particle diameters of typically 29 nm (close to the nominal particle size, 35 nm, for this commercial nano-material). With platinum nanoparticles "photo-attached" onto the ZnO nanoparticles (by photoconversion of Pt^{4+} to Pt^0 when stirring a suspension of ZnO and K_2PtCl_6, see experimental) a grey powder (in contrast to white ZnO) is obtained. Formation of platinum is confirmed in Fig. 4C as dark dots attached to the ZnO with an average particle size of 3.2 nm (Fig. 4D). XRD measurements were performed (see Fig. 4E) in order to determine the crystalline phase of these materials. For both materials ZnO and Pt@ZnO the same diffraction peaks for the hexagonal wurtzite phase were confirmed in good agreement with 36-1451 standard data from the JCPDS data base with strong and sharp diffraction peaks at 2θ = 31.7°, 34.4°, 36.2°, 47.5°, 56.8°, 62.9°, 66.4°, 68.0°, 69.1°, 72.5°,

77.1°, 81.3°, 89.6°, 92.8° corresponding to crystalline planes (100), (002), (101), (102), (110), (103), (200), (112), (201), (004), (202), (104), (203) and (210), respectively [17]. It is noteworthy that no diffraction peaks for Pt are detected in the Pt@ZnO material, which is mainly due to the low volume of Pt and the small crystal size for Pt deposited onto the ZnO nanoparticles. Similar behaviour also was noted by Li *et al*. [10].

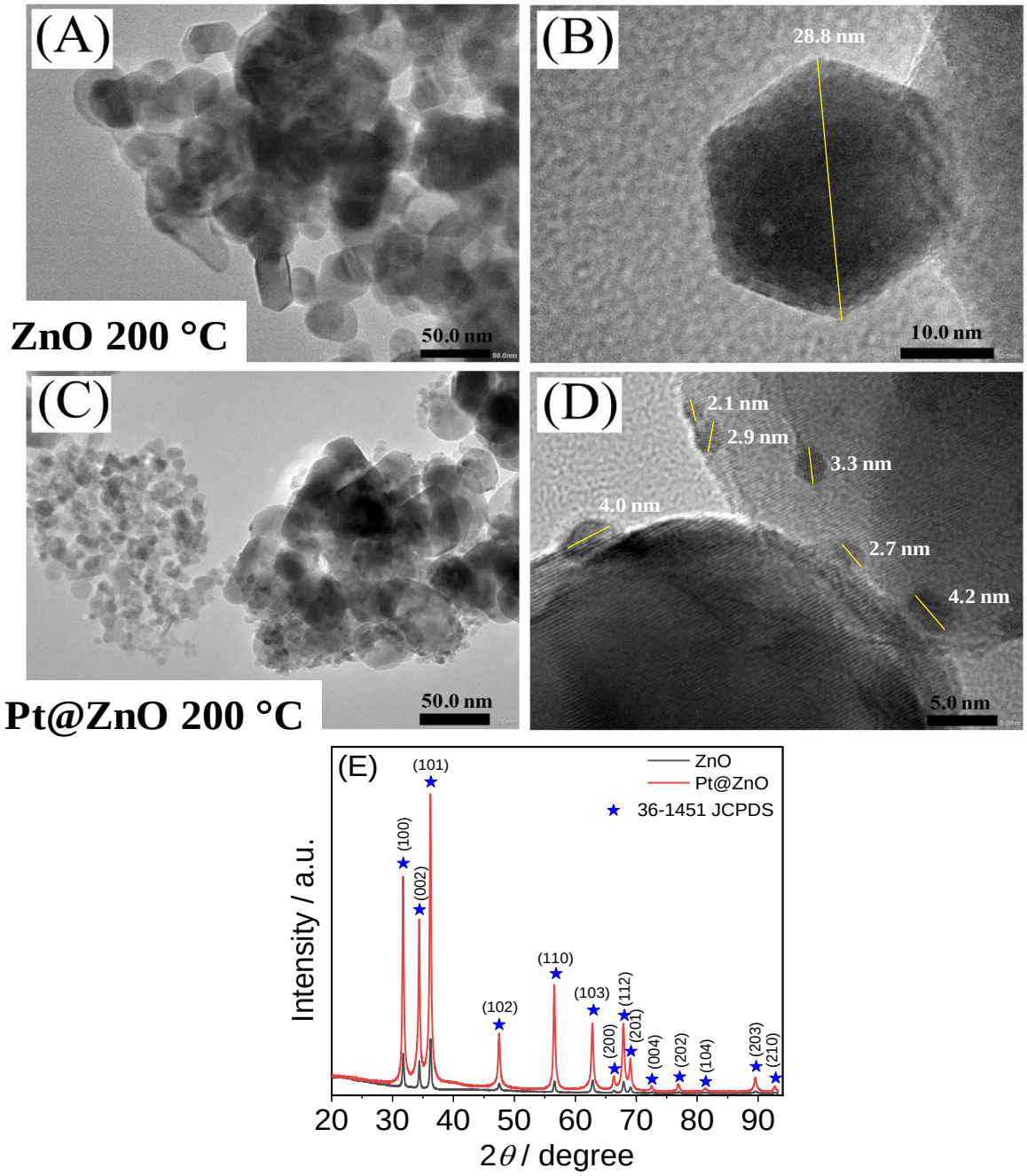

Figure 4 – Transmission electron micrograph (TEM) images for ZnO (A, B) and for Pt@ZnO (C, D); X-ray diffractogram of ZnO and Pt@ZnO (E). Both samples were previously heat treated at 200 °C.

The elemental mappings and composition of the materials were measured by energy dispersive X-ray analysis (EDX) and are shown in the Fig. 5. The spectra in Fig.5A and 5E show in % atomic elements O and Zn (with C, Cr, Cu due to the substrate). Pt is observed in Fig. 5E. Fig. 5B – 5D and Fig. 5F – 5H show elemental mappings for both materials. Nanoparticles of Pt are homogenously distributed over the bigger ZnO nanoparticles.

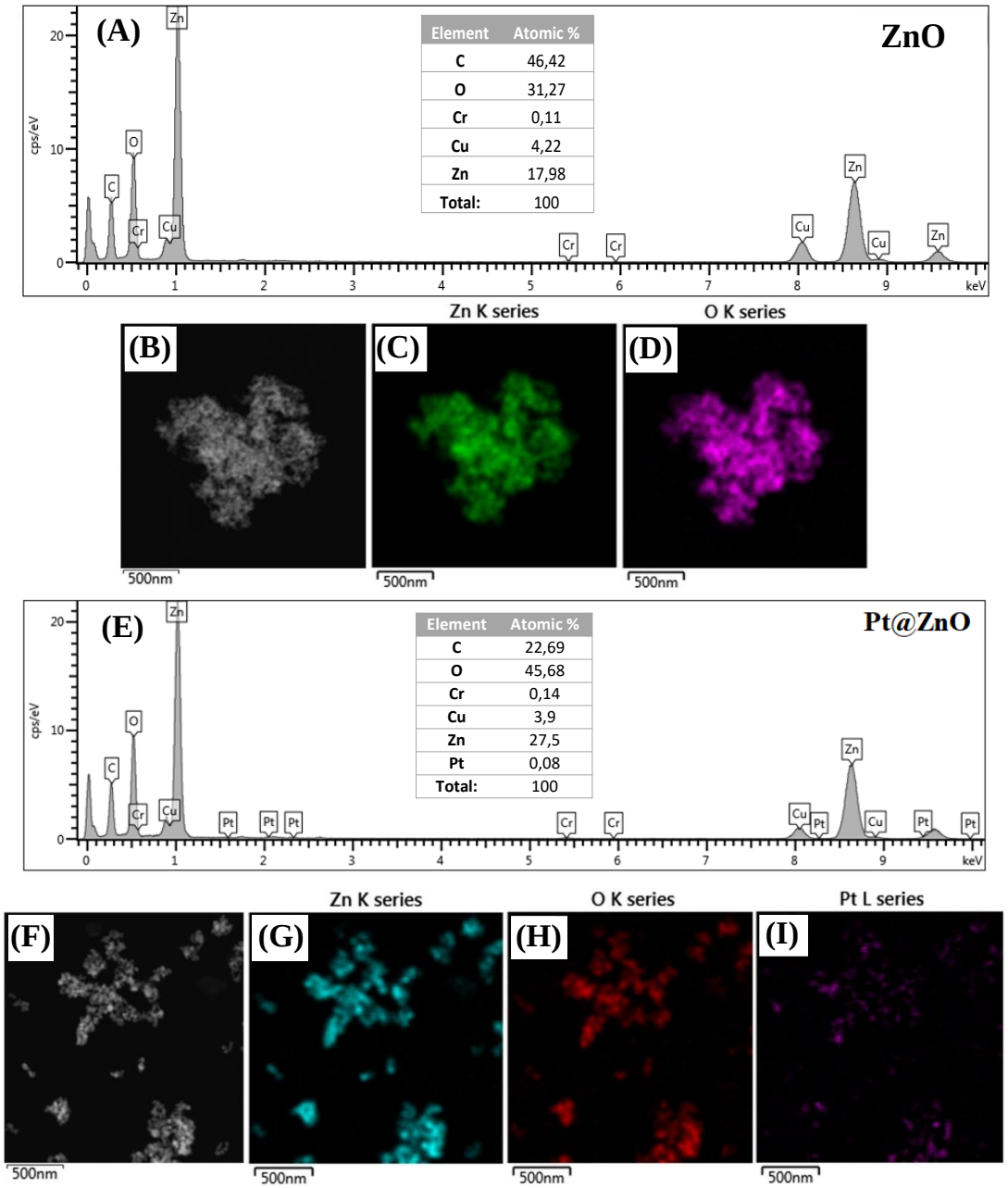

Figure 5 – Energy dispersive X-ray spectroscopy (EDX) data and mapping for the ZnO (A-D) and for Pt@ZnO (E-I).

206

207 **3.2. Photoelectrochemical Characterisation of Pt@ZnO and ZnO Nanophotocatalysts**

208 In initial photoelectrochemical experiments, the selected electrolyte was 10 mmol L^{-1}
209 phosphate buffer solution at pH 7 containing 500 mmol L^{-1} glucose as the hole quencher. A
210 volume of 8 μL of Pt@ZnO suspension (48 μg Pt@ZnO) was deposited onto either glassy
211 carbon or platinum disk electrodes. Data in Fig. S3 show that only very poor photo-
212 electrochemical responses are observed for both types of electrodes. For the platinum electrode
213 the photo-electrochemical responses were more significant (Fig. S3B), but also rapidly
214 decaying after three voltammetric cycles. This is tentatively assigned to phosphate-induced
215 inactivation/modification of the Pt@ZnO surface. According to Hermann *et al*. [18], zinc oxide
216 nanoparticles are highly sensitive towards phosphate anions even at pH 7.

217

218 To avoid this problem, the phosphate buffer solution was replaced by aqueous 10 mmol
219 L^{-1} NaCl. Exploratory experiments were carried out with Pt@ZnO nanoparticles in 10 mmol
220 L^{-1} NaCl to assess the effects of the amount of deposition and the concentration of glucose hole
221 quencher. Fig. 6A shows cyclic voltammetry data obtained under pulsed light conditions (λ =
222 385 nm; 1 s off 2 s on; approx. 100 $mWcm^{-2}$) for electrodes immersed in 10 mmol L^{-1} NaCl
223 with varying concentrations of 0 – 1000 mmol L^{-1} glucose. The photocatalyst, 48 μg Pt@ZnO,
224 is deposited onto a 3 mm diameter platinum disc electrode and an onset of photocurrents is
225 observed at -0.6 V *vs.* SCE (see Fig. 6A). With a more positive applied voltage, the
226 photocurrent responses increase reaching approx. 190 μA at 0.6 V *vs.* SCE (corresponding to
227 2.7 $mAcm^{-2}$). These are substantial photocurrent responses and the effect of glucose
228 concentration (Fig. 6B) suggests that glucose acts as a quencher of holes. An optimum
229 photocurrent response is observed with 500 mmol L^{-1} glucose (see Fig. 6B). When varying the
230 amount of photocatalyst on the electrode surface, 8 μL (or 48 μg) Pt@ZnO on the 3 mm
231 diameter electrode surface appears to provide optimum conditions for maximum photocurrent
232 generation (Fig. 6C).

233

234

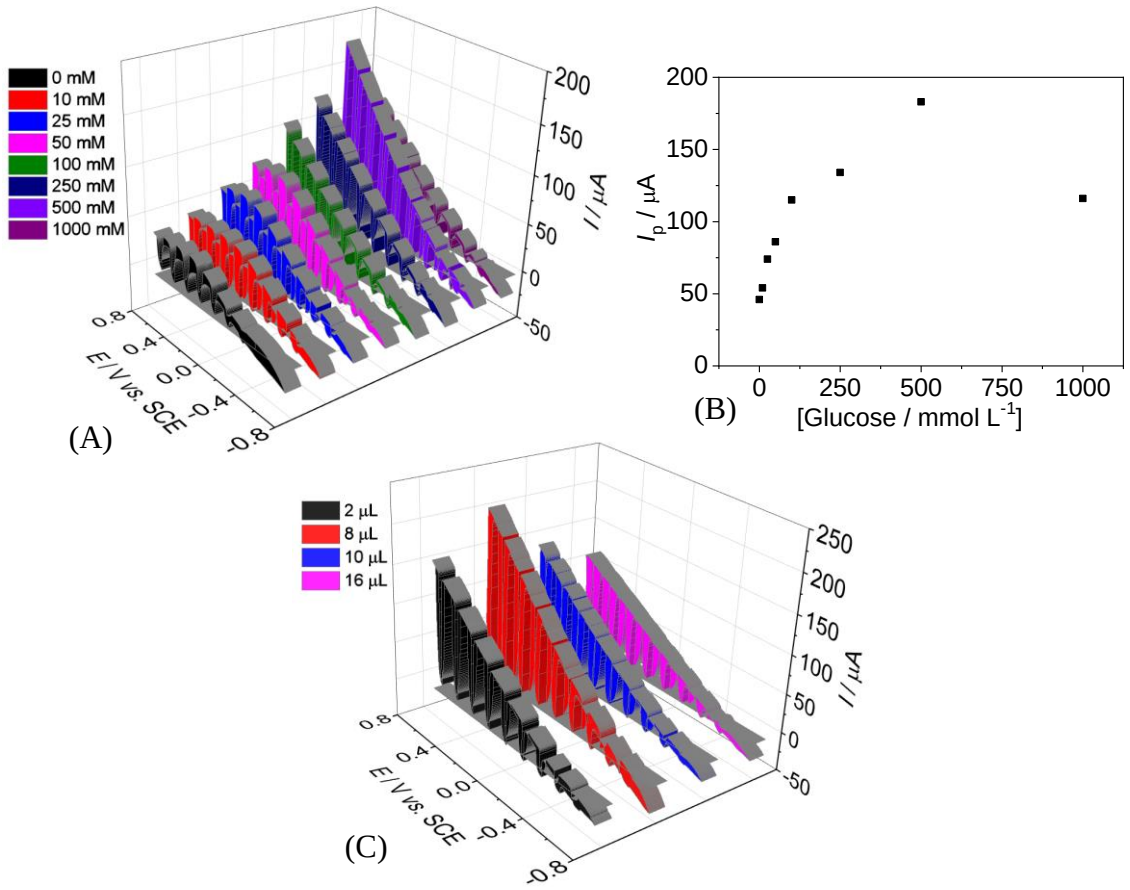

Figure 6 – 3D graphic of current *vs*. potential data from cyclic voltammetry experiments (scan rate 50 mVs^{-1}; 3 mm diameter Pt electrode) for different concentrations of glucose in 10 mmol L^{-1} NaCl with pulse of light of 1s off and 2 s on using a power LED λ = 385 nm (A). Plot of I_p *vs.* concentration of glucose (B). 3D graphic with cyclic voltammetry data for the optimization of the mass of Pt@ZnO electrode (1 µL equals 6 µg Pt@ZnO) (C).

Photocurrents are generated starting at an onset potential of -0.6 V *vs.* SCE, and a proposed mechanism can be expressed as a sequence of excitation and charge separation (equation 1), hole quenching by glucose forming gluconic acid (equation 2), hydrogen formation (equation 3) and discharge (equation 4). Alternatively, the electrons could diffuse through the ZnO towards the electrode (equation 5). Similar reaction schemes can be written either for Pt@ZnO or for ZnO.

$$Pt@ZnO + h\nu \longrightarrow Pt^{-}@ZnO^{+} \quad (1)$$

$$2\ Pt^{-}@ZnO^{+} + H_2O + \text{glucose} \longrightarrow 2\ Pt^{-}@ZnO + \text{gluconic acid} + 2H^{+} \quad (2)$$

$$2\ Pt^{-}@ZnO + 2\ H^{+} \longrightarrow 2\ Pt@ZnO + H_2(aq) \quad (3)$$

$$H_2(aq) \longrightarrow 2\ H^{+}(aq) + 2\ e^{-}(Pt) \quad (4)$$

$$Pt^{-}@ZnO \longrightarrow Pt@ZnO + e^{-}(Pt) \quad (5)$$

In order to better understand the underlying processes, both Pt@ZnO and ZnO are investigated and compared without heat treatment, with 200 and 400 °C heat treatment, and in the presence of argon/absence of O_2. Data in Fig. 7B and 7F demonstrate that an initial gentle heat treatment of the photocatalyst powder can be used to stabilise the photo-current responses. A treatment for 2 h at 200 °C leads to well-defined photocurrents, whereas treatment at 400 °C (Fig. 7C, G) clearly causes detrimental effects on the photo-redox process. Given that there is no significant change in the electron optical data for photocatalyst before and after 200 °C heat treatment, it seems likely that these effects are linked to surface conditioning (dehydration) or inter-grain contacts. This in turn could affect either chemical/catalytic reactivity of the surface or electron transport properties across grain boundaries in the ambiently deposited photocatalysts. Therefore, 200 °C heat treatment can "condition" the ZnO surface to maintain activity.

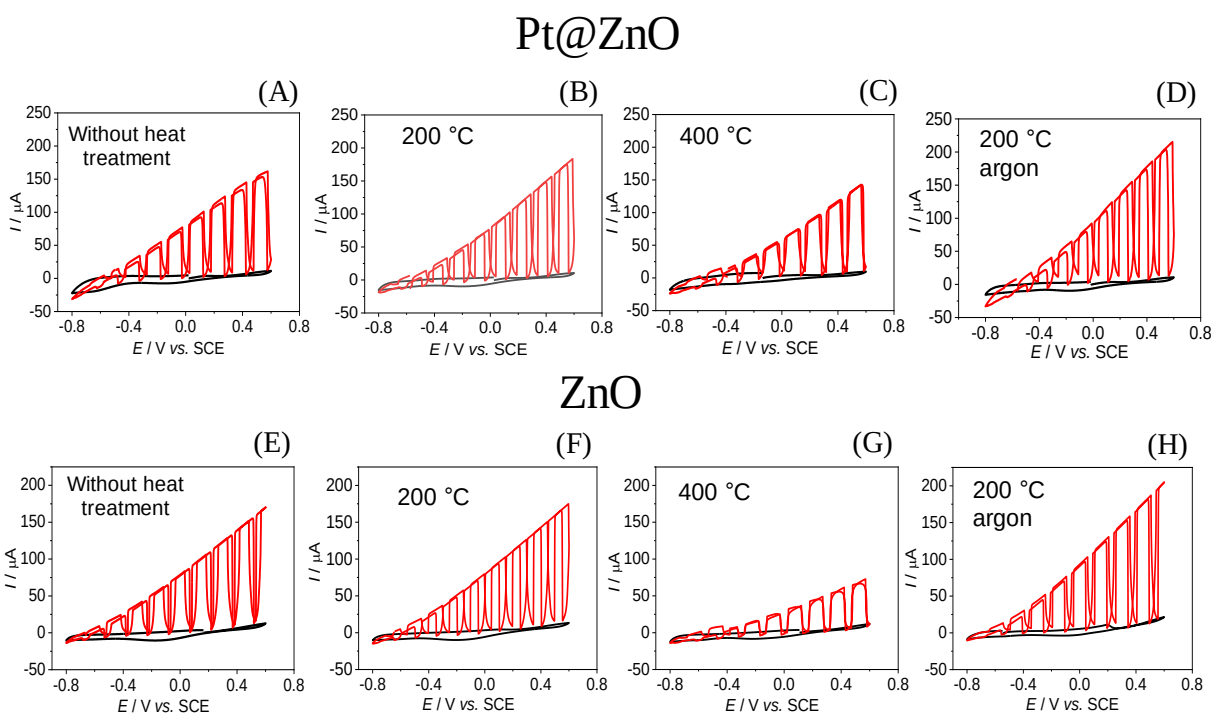

Figure 7 – Cyclic voltammetry data (scan rate 50 mVs^{-1}; 3 mm diameter Pt electrode) showing the influence of the heat treatment in the current of the Pt@ZnO/Pt electrode in 10 mmol L^{-1} NaCl + 500 mmol L^{-1} glucose without and with pulsed light (1s off and 2 s on; λ = 385 nm) in air (A-C) and under argon (D). Influence of the heat treatment in the current of the ZnO/Pt electrode in 10 mmol L^{-1} NaCl + 500 mmol L^{-1} glucose without and with pulsed light in air (E-G) and under argon (H).

Fig. 7D and 7H show data for experiments comparing argon de-aerated electrolyte with ambient oxygen containing electrolyte (7B, 7F). Only a minor improvement is observed for both Pt@ZnO and for ZnO photocatalyst materials. This can be attributed to O_2 absence stopping recombination losses with hydrogen or electrons. When investigating the reactivity of ZnO *versus* that of Pt@ZnO the similarity of the photocurrent data is striking. Does the platinum deposit really affect the mechanism under these conditions? Therefore, it is of interest to explore substrate electrodes other than platinum (platinum was chosen initially to capture hydrogen). Fig. 8 shows voltammetry data obtained with pulsed light for Pt@ZnO (A, B) and for ZnO (C, D) deposited on a 3 mm diameter glassy carbon disc electrode and immersed into 10 mmol L^{-1} NaCl with 500 mmol L^{-1} glucose. Both the Pt@ZnO and the ZnO photocatalyst give similar photo-current responses. This observation strongly points to a mechanism that doesn't require platinum as catalyst and therefore, the mechanism is based predominantly on electron transport (see equation 4) as opposed to the hydrogen diffusional transport (see equation 3).

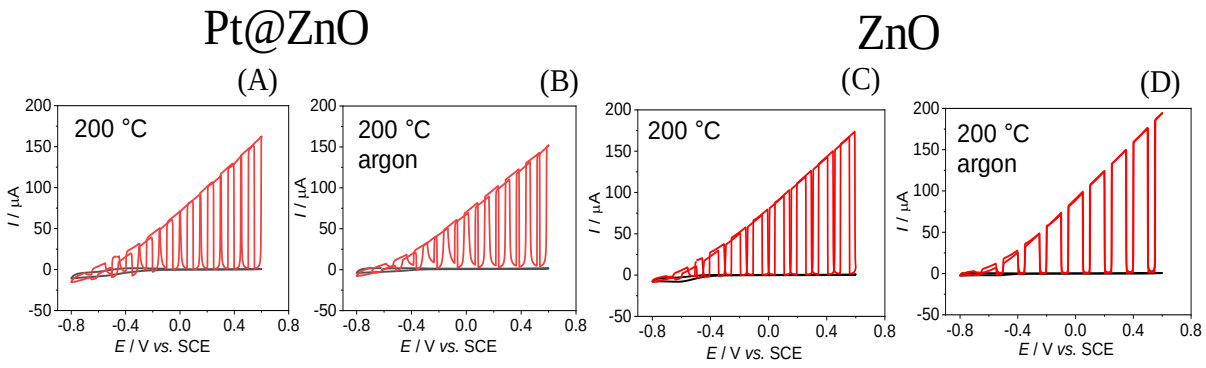

Figure 8 – Current *vs.* potential data from cyclic voltammetry experiments (scan rate 50 mVs^{-1}; 3 mm diameter glassy carbon) for a Pt@ZnO/GC electrode immersed in 10 mmol L^{-1} NaCl + 500 mmol L^{-1} glucose without and with pulsed light (1s off and 2 s on; λ = 385 nm) in air (A) and under argon (B). As above, but for a ZnO/GC electrode immersed in 10 mmol L^{-1} NaCl + 500 mmol L^{-1} glucose in air (C) and under argon (D).

Further investigation of the mechanism is possible by intentionally purging the solution with hydrogen gas. Data in Fig. 9A show the photo-current responses (red) and the dark current (black) for ZnO on glassy carbon in 10 mmol L^{-1} NaCl with 500 mmol L^{-1} glucose. The dark current is shown more clearly in Fig. 9B for potential cycle 1, 5, and 10. The cathodic current shows an onset at approx. -0.6 V *vs.* SCE with a current associated mainly with oxygen

reduction. In the presence of argon, the photo-current responses remain similar (Fig. 9C) but the dark currents are simplified to only the response for the nano-ZnO semiconductor. At a potential of approx. -0.6 V *vs.* SCE a cathodic peak is followed by a chemically reversible reduction/re-oxidation feature consistent with the ZnO surface state reduction and reversible filling of the ZnO conduction band (in the presence of glucose). This behaviour is retained under an atmosphere of hydrogen (Fig. 9E, 9F), which clearly shows that hydrogen is not an intermediate in this process (that is, the process in equation 3 can be ruled out under these conditions). Hydrogen oxidation (under hydrogen atmosphere) was observed only for the platinum disc electrodes or for Pt@ZnO coated glassy carbon electrodes (see Fig. S4). The approximate (poorly defined) equilibrium potential (measured at a platinum disk) for hydrogen in 10 mmol L^{-1} NaCl with 500 mmol L^{-1} glucose was at approx. -0.5 V *vs*. SCE (see Fig. S4). Perhaps interestingly, somewhat lower photocurrents are observed also in the absence of glucose and under hydrogen (Fig. 9G, H) and similar currents are seen also in ambient oxygen in the absence of glucose (not shown). It can be concluded that some oxygen (either ambient in solution or generated at the semiconductor surface) can be tolerated in this process. The somewhat lower plateauing photocurrent and shift in onset potential can be attributed to the absence of hole quencher.

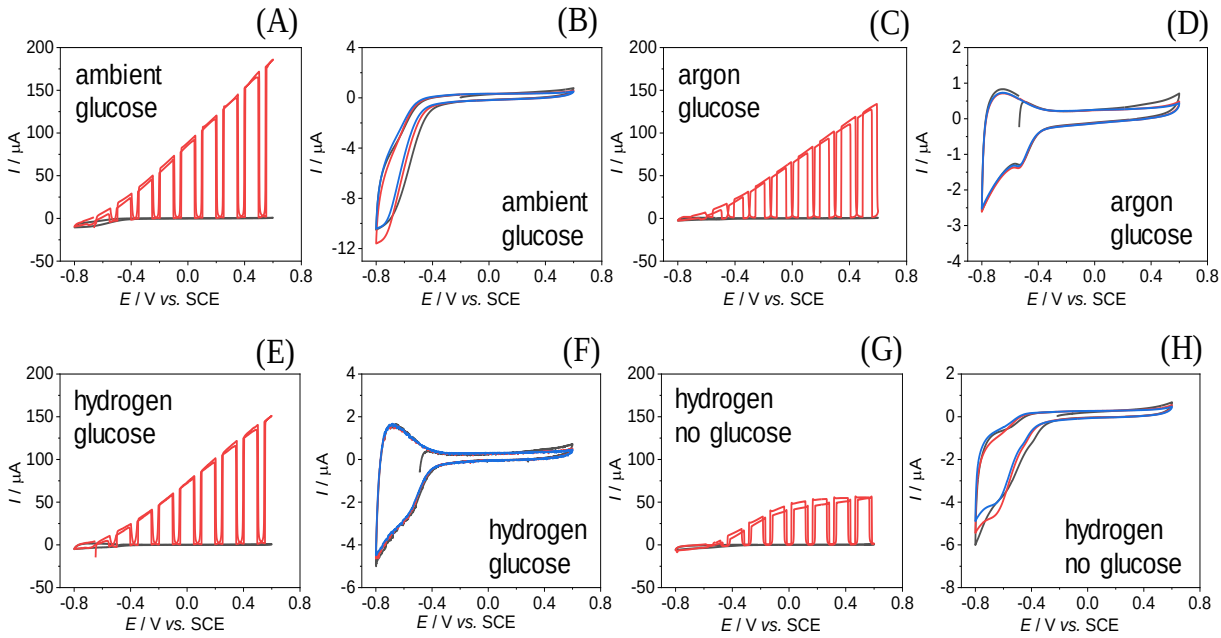

Figure 9 – Cyclic voltammetry data (scan rate 50 mVs^{-1}; 3 mm diameter glassy carbon) showing the influence of environment on the photocurrent for ZnO/GC electrode in 10 mmol L^{-1} NaCl + 500 mmol L^{-1} glucose without and with pulsed light (1s off and 2 s; λ = 385 nm) in air (A, B), under argon (C, D), under hydrogen (E, F), and under hydrogen without glucose (G,

H). Also shown are cyclic voltammograms without pulse of light (B, D, F and H) 1st cycle (–), 5th cycle (–) and 10th cycle (–).

Photocurrent responses from both Pt@ZnO and from ZnO (after 200 °C heat treatment) are reasonably robust but do decay with prolonged operation (or also for lower glucose concentrations). Fig. 10 shows data for up to 5 repeat voltammograms for Pt@ZnO and ZnO and for both glassy carbon and platinum disk electrode substrates. In all cases a gradual change occurs, and plateauing is observed. Glassy carbon electrodes seem to perform better when compared to platinum electrodes. Given the surface sensitivity of the overall photo-redox process, it seems likely that the degradation of the photocurrents is linked to species absorbed to the ZnO surface. Glucose adsorption itself may play a role and the adsorption of reaction products such as gluconic acid.

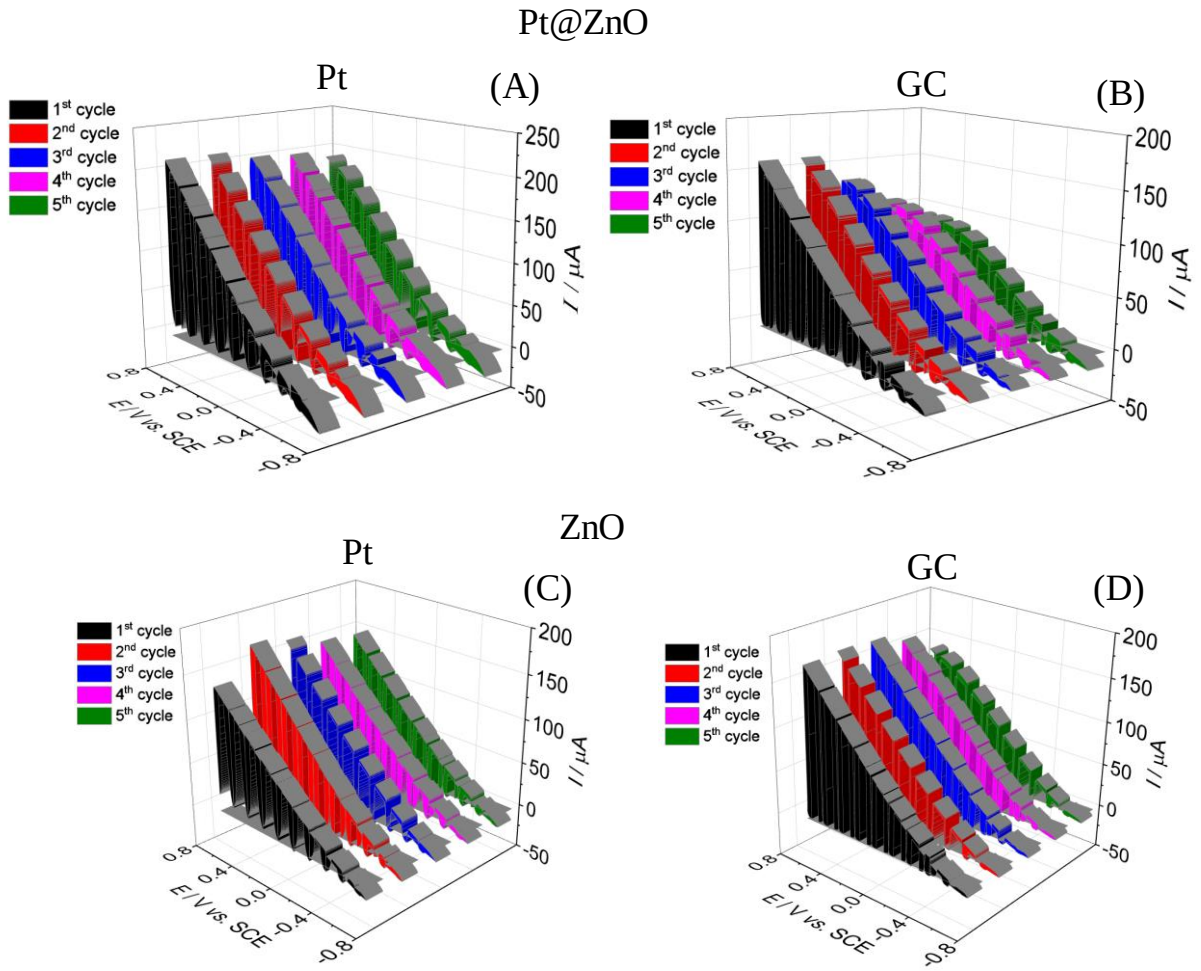

Figure 10 – Cyclic voltammetry (scan rate 50 mVs^{-1}; 3 mm diameter Pt or GC electrode; using pulsed light 1s off and 2 s on; λ = 385 nm) for 48 µg of Pt@ZnO or ZnO deposits (both with

200 °C heat treatment) on the electrode immersed in 10 mmol L^{-1} NaCl + 500 mmol L^{-1} glucose. (A) Pt@ZnO/Pt, (B) Pt@ZnO/GC, (C) ZnO/Pt, (D) ZnO/GC.

These data show that the photo-redox process based on photoexcitation of ZnO in the presence of glucose is very similar on both platinum or glassy carbon. Most likely, ZnO after excitation undergoes hole quenching, and then conduction of electrons in ZnO towards the underlying electrode occurs. However, the conduction band electrons from ZnO can still be harvested in the form of hydrogen (*vide infra*). Next, an indirect photoelectrochemical system is investigated based on a palladium membrane electrode. This type of electrode allows the photochemical generation of hydrogen (or conduction band electrons) to be separated from the electrochemical electricity generation. Figure 11A shows a schematic drawing of the indirect photoelectrochemical system.

3.3. Indirect Photoelectrochemical Energy Conversion with ZnO and Pt@ZnO Nanophotocatalysts

Palladium films are known to absorb hydrogen and to allow rapid diffusion of hydrogen across to the opposite side of a thin membrane [15]. Here, a commercial 0.025 mm thick palladium membrane is employed. It has been shown that the diffusion coefficient for hydrogen in palladium or in palladium alloys is approximately $D = 10^{-11}$ m^2 s^{-1} [19] at room temperature. Therefore, the transport time for hydrogen diffusing through a membrane of thickness L = 0.025 mm can be estimated as typically $\tau \approx L^2/D \approx 62$ s [20].

Data in Figure 11B show chronopotentiometry transients for a palladium membrane electrode (exposed area 2 mm diameter) exposed to 500 mmol L^{-1} glucose in water. Both ZnO and Pt@ZnO provide photo-potential transients within a “switch-on” period of typically 1-2 minutes after switching on the light source. In the presence of ambient oxygen or in the presence of argon Pt@ZnO seems to perform slightly better giving a more negative steady state equilibrium potential after a period of 1000 s. The anticipated equilibrium potential for a H_2/O_2 electrolytic cell at 1 bar pressure would be 1.23 V [21], but here the oxygen pressure is lower and, more importantly, the hydrogen pressure locally at the palladium surface (facing into the electrochemical cell) is substantially lower due to the binding of hydrogen into the palladium [22]. The presence of oxygen on both sides of the palladium membrane also affects the apparent

equilibrium pressure. De-aerating with argon on the electrolyte side where the electrochemical process occurs (see Figure 12B) improves the photo-potential to approx. - 0.8 V, but losses due to oxygen and the hydrogen concentration gradient through the palladium membrane are still limiting factors.

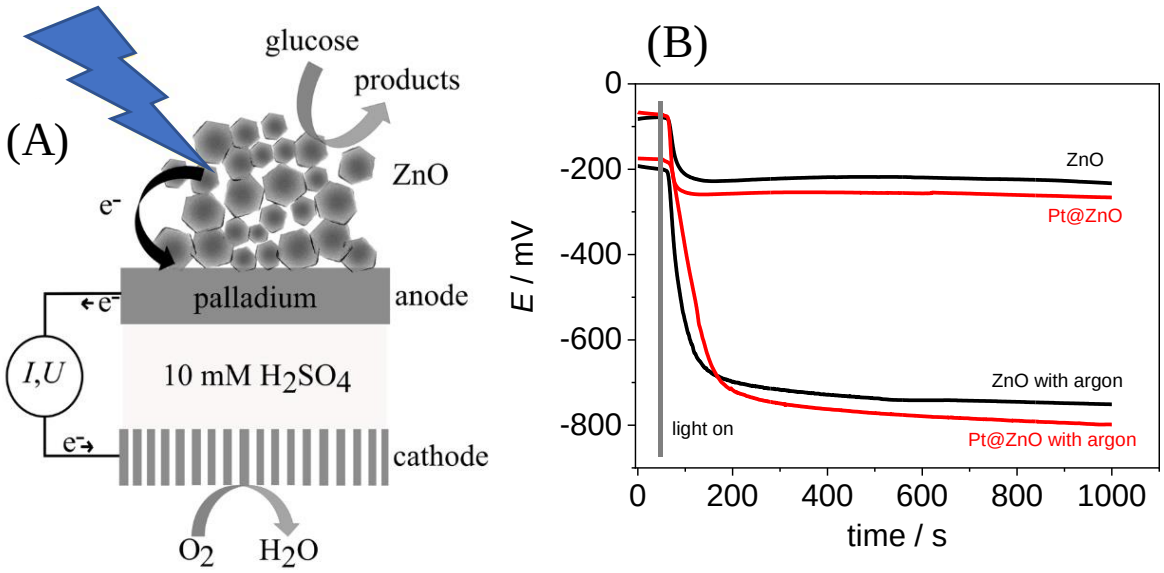

Figure 11 – (A) Schematic drawing of the indirect photoelectrochemical cell with 10 mmol L^{-1} NaCl and 500 mmol L^{-1} glucose in the photocatalysis compartment and 10 mmol L^{-1} H_2SO_4 in the electrochemical compartment. (B) Zero current chronopotentiometry data for 24 µg ZnO or Pt@ZnO deposited onto a palladium membrane (2 mm diameter) in air and under argon (on the side of the electrolyte) using a 3D-printed fuel cell (see experimental). Light was switched on at 50 s.

The generation of hydrogen at the palladium membrane is clearly detected. The fact that hydrogen is generated must be linked to the production of electrons in the ZnO deposit (Fig. 11A, *vide supra*). These electrons lower the work-function of the palladium and then lead to proton uptake to give interstitial hydrogen in the palladium lattice. The overall process can lead to an indirect photocurrent as is shown in Fig. 12. Fig. 12A shows cyclic voltammetry data (under constant illumination) and in ambient air conditions. From the apparent equilibrium potential (OCP) at -0.25 V, the potential is slowly scanned positive (into the power generation region). The same data when plotted as power *versus* potential (Fig.12C) shows that the Pt@ZnO photocatalyst performs slightly better with maximum power of 20 nW (or 0.63 µW cm^{-2}). Under argon atmosphere in Fig. 12D (with argon in the electrochemical compartment; this is more effective compared to purging with argon in the photocatalysis compartment) the

cyclic voltammetry response starts at approx. -0.8 V and reaches higher currents, but then shows depletion effects and a collapse in current at lower voltages. The corresponding power output peaks at 0.9 µW (or 28 µW cm^{-2}). Here, the Pt@ZnO photocatalyst clearly outperforms the ZnO photocatalyst. The reasons for this and the effects introduced by the palladium interface will require further study. The rather limited generation of power is likely to be linked to the performance of the photocatalyst and additional impedance introduced by the palladium membrane. In the future, improvements will be possible.

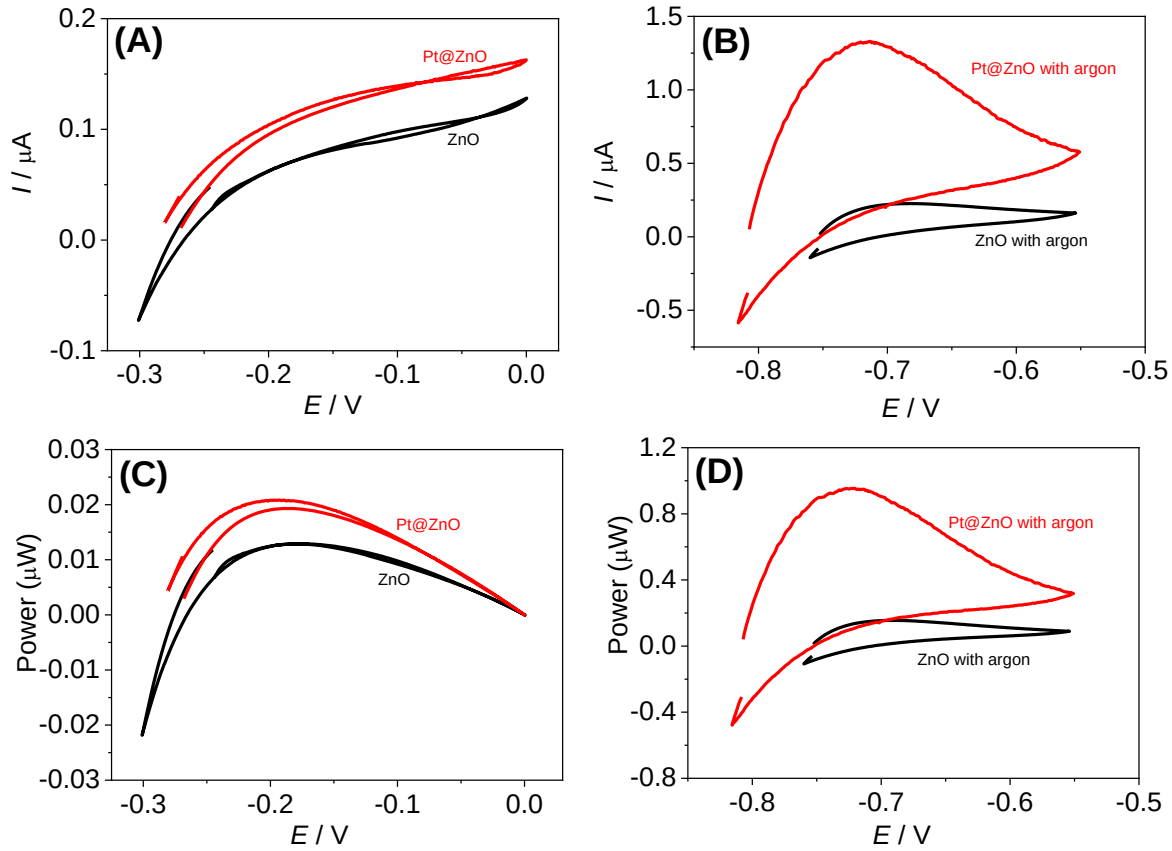

Figure 12 – (A, B) Cyclic voltammetry (scan rate 1 mVs^{-1}) starting at OCP. A deposit of 24 µg ZnO or Pt@ZnO on a palladium membrane was employed in air (A) and under argon (B). (C, D) Power plots (power = current × voltage) due to indirect H_2 generation measured in the 3D-printed photo-fuel cell in air (C) and with argon de-aeration in the electrochemical compartment (D).

4. Conclusion

It has been shown that commercial nano-ZnO (with approx. 29 nm diameter) ambiently deposited onto platinum or glassy carbon disc electrodes can be used for photo-current generation. Glucose added as hole quencher (here employed to mimic biomass) substantially

increases the anodic photocurrents, but operation in the absence of glucose (in aqueous 10 mmol L^{-1} NaCl) is also possible. Perhaps surprisingly, both ZnO and Pt@ZnO perform equally well, which is indicative for an electron transport mechanism in ZnO, rather than a hydrogen intermediated mechanism in the surrounding solution. This was further confirmed with experiments performed under hydrogen atmosphere, which allowed formation of hydrogen at the ZnO surface to be ruled out. However, hydrogen was formed when conduction band electrons in ZnO reached the surface of a palladium membrane. This was shown by monitoring photo-potentials and photocurrents in an indirect photo-electrochemical cell. Power-generation was demonstrated. However, more work will be necessary to improve the performance and to better understand the power-limiting photo-current inhibition effects in the mechanism. The ZnO surface seems to play an important role with both glucose adsorption and possibly gluconic acid absorption affecting the processes. More work will be needed to explore the effects of simple molecules such as glucose on the fate of the conduction band electrons in ZnO.

Indirect photoelectrochemical system are attractive due to the separation of the photocatalysis and the electrolytic power generation. The photocatalytic process when separated does not require electrolyte and could be performed in complex waste media. However, a much better design will be necessary for higher power output and crucially, the palladium membrane needs to be replaced with hybrid materials or composites to perform better and at lower costs. To develop better indirect photo-electrochemical fuel cells in the future, it will be necessary to also develop (A) more stable photocatalysts, (B) improved light absorbers by better interfacial design, and (C) new photocatalysts that allow hydrogen intermediate production and capture under illumination and in the presence of hole quenchers [12]. Hydrogen as a reaction intermediate is more likely to be transferred effectively (from further distance) to the palladium membrane when compared to conduction band electrons in the nanoparticulate ZnO semiconductor.

Acknowledgements

The authors are grateful to FAPESP (#2014/50945-1) and INCT-DATREN (#465571/2014-0) for support for this work. K.I. received a scholarship from FAPESP (#2019/07020-3).

References

[1] R. Ramachandran, R.K. Menon, An overview of industrial uses of hydrogen, Int. J. Hydrog. Energy. 23 (1998) 593–598. https://doi.org/10.1016/S0360-3199(97)00112-2.

[2] J.D. Holladay, J. Hu, D.L. King, Y. Wang, An overview of hydrogen production technologies, Catal. Today. 139 (2009) 244–260. https://doi.org/10.1016/j.cattod.2008.08.039.

[3] S.N. Paglieri, J.D. Way, Innovations in Palladium Membrane Research, Sep. Purif. Methods. 31 (2002) 1–169. https://doi.org/10.1081/SPM-120006115.

[4] S. Yun, S. Ted Oyama, Correlations in palladium membranes for hydrogen separation: A review, J. Membr. Sci. 375 (2011) 28–45. https://doi.org/10.1016/j.memsci.2011.03.057.

[5] J. Zhang, L. Sun, K. Ichinose, K. Funabiki, T. Yoshida, Effect of anchoring groups on electrochemical self-assembly of ZnO/xanthene dye hybrid thin films, Phys. Chem. Chem. Phys. 12 (2010) 10494. https://doi.org/10.1039/c002831b.

[6] C. Xia, Z. Qiao, C. Feng, J.-S. Kim, B. Wang, B. Zhu, Study on Zinc Oxide-Based Electrolytes in Low-Temperature Solid Oxide Fuel Cells, Materials. 11 (2018) 40. https://doi.org/10.3390/ma11010040.

[7] A.B. Djurišić, X. Chen, Y.H. Leung, A.M.C. Ng, ZnO nanostructures: growth, properties and applications, J. Mater. Chem. 22 (2012) 6526–6535. https://doi.org/10.1039/C2JM15548F.

[8] J. Fang, H. Fan, Y. Ma, Z. Wang, Q. Chang, Surface defects control for ZnO nanorods synthesized by quenching and their anti-recombination in photocatalysis, Appl. Surf. Sci. 332 (2015) 47–54. https://doi.org/10.1016/j.apsusc.2015.01.139.

[9] T. Xu, L. Zhang, H. Cheng, Y. Zhu, Significantly enhanced photocatalytic performance of ZnO via graphene hybridization and the mechanism study, Appl. Catal. B Environ. 101 (2011) 382–387. https://doi.org/10.1016/j.apcatb.2010.10.007.

[10] Z. Li, Z. Liu, B. Li, D. Li, Y. Fang, Low-loading platinum decorated aligned ZnO nanorods and their photocatalytic and electrocatalytic applications, J. Mater. Sci. Mater. Electron. 26 (2015) 3909–3915. https://doi.org/10.1007/s10854-015-2918-2.

[11] K. Abdul Razak, S.H. Neoh, N.S. Ridhuan, N. Mohamad Nor, Effect of platinum-nanodendrite modification on the glucose-sensing properties of a zinc-oxide-nanorod electrode, Appl. Surf. Sci. 380 (2016) 32–39. https://doi.org/10.1016/j.apsusc.2016.02.091.

[12] (a) Y. Zhao, N.A. Al Abass, R. Malpass-Evans, M. Carta, N.B. McKeown, E. Madrid, P.J. Fletcher, F. Marken, Photoelectrochemistry of immobilised Pt@g-C_3N_4 mediated by hydrogen and enhanced by a polymer of intrinsic microporosity PIM-1, Electrochem. Commun. 103 (2019) 1–6. https://doi.org/10.1016/j.elecom.2019.04.006. (b) Y. Zhao, J. Dobson, C. Harabajiu, E. Madrid, T. Kanyanee, C. Lyall, S. Reeksting, M. Carta, N.B. McKeown, L. Torrente-Murciano, K. Black, F. Marken, Indirect photo-electrochemical detection of carbohydrates with Pt@g-C_3N_4 immobilised into a polymer of intrinsic

microporosity (PIM-1) and attached to a palladium hydrogen capture membrane, Bioelectrochem. 134 (2020) 107499. https://doi.org/10.1016/j.bioelechem.2020.107499.

[13] Y.-K. Hsu, S.-Y. Fu, M.-H. Chen, Y.-C. Chen, Y.-G. Lin, Facile Synthesis of Pt Nanoparticles/ZnO Nanorod Arrays for Photoelectrochemical Water Splitting, Electrochimica Acta. 120 (2014) 1–5. https://doi.org/10.1016/j.electacta.2013.12.095.

[14] T. Graham, XXXVI.—On the relation of hydrogen to palladium, J. Chem. Soc. 22 (1869) 419–432. https://doi.org/10.1039/JS8692200419.

[15] T.L. Ward, T. Dao, Model of hydrogen permeation behavior in palladium membranes, J. Membr. Sci. 153 (1999) 211–231. https://doi.org/10.1016/S0376-7388(98)00256-7.

[16] R.A. Escalona-Villalpando, A. Dector, D. Dector, A. Moreno-Zuria, S.M. Durón-Torres, M. Galván-Valencia, L.G. Arriaga, J. Ledesma-García, Glucose microfluidic fuel cell using air as oxidant, Int. J. Hydrog. Energy. 41 (2016) 23394–23400. https://doi.org/10.1016/j.ijhydene.2016.04.238.

[17] N.A. Al-Shabib, F.M. Husain, F. Ahmed, R.A. Khan, I. Ahmad, E. Alsharaeh, M.S. Khan, A. Hussain, M.T. Rehman, M. Yusuf, I. Hassan, J.M. Khan, G.M. Ashraf, A. Alsalme, M.F. Al-Ajmi, V.V. Tarasov, G. Aliev, Biogenic synthesis of Zinc oxide nanostructures from Nigella sativa seed: Prospective role as food packaging material inhibiting broad-spectrum quorum sensing and biofilm, Sci. Rep. 6 (2016) 36761. https://doi.org/10.1038/srep36761.

[18] R. Herrmann, F.J. García-García, A. Reller, Rapid degradation of zinc oxide nanoparticles by phosphate ions, Beilstein J. Nanotechnol. 5 (2014) 2007–2015. https://doi.org/10.3762/bjnano.5.209.

[19] R.V. Bucur, The Influence of Experimental Conditions upon the Measurements of Hydrogen Diffusion in Palladium by Electrochemical Permeation Methods*, Z. Für Phys. Chem. 146 (1985) 217–229. https://doi.org/10.1524/zpch.1985.146.2.217.

[20] Y. Liu, Y. Li, P. Huang, H. Song, G. Zhang, Modeling of hydrogen atom diffusion and response behavior of hydrogen sensors in Pd–Y alloy nanofilm, Sci. Rep. 6 (2016) 37043. https://doi.org/10.1038/srep37043.

[21] C. Wei, R.R. Rao, J. Peng, B. Huang, I.E.L. Stephens, M. Risch, Z.J. Xu, Y. Shao-Horn, Recommended Practices and Benchmark Activity for Hydrogen and Oxygen Electrocatalysis in Water Splitting and Fuel Cells, Adv. Mater. 31 (2019) 1806296. https://doi.org/10.1002/adma.201806296.

[22] E. McCafferty, Thermodynamics of Corrosion: Pourbaix Diagrams, in: E. McCafferty (Ed.), Introd. Corros. Sci., Springer, New York, NY, 2010: pp. 95–117. https://doi.org/10.1007/978-1-4419-0455-3_6.